RESEARCH ARTICLE
PLANETARY SCIENCES

Earth and Planetary Physics
*9*: 357–365, 2025
doi: 10.26464/epp2025027

# Modulation of suprathermal electron fluxes by ultra-low-frequency magnetic field fluctuations in the Martian foreshock

**TaiFeng Jin*, BinBin Ni*, Song Fu, XiaoTong Yun, ShuYue Pang, MinYi Long, QiongYue Zhang, Nan Wang, XinJie Xiong, YiBin Zhao, and FangFei Shi**

School of Earth and Space Science and Technology, Wuhan University, Wuhan 430072, China

**Key Points:**

- Electron fluxes at ~10–100 eV are observed to be modulated by ultra-low-frequency (ULF) waves upstream of the Martian bow shock.
- The electron flux enhancements in a perpendicular direction show close correlations with the ULF magnetic field fluctuations.
- Interactions between suprathermal electrons and ULF waves may be a general process in space plasmas.

**Citation:** Jin, T. F., Ni, B. B., Fu, S., Yun, X. T., Pang, S. Y., Long, M. Y., Zhang, Q. Y., Wang, N., Xiong, X. J., Zhao, Y. B., and Shi, F. F. (2025). Modulation of suprathermal electron fluxes by ultra-low-frequency magnetic field fluctuations in the Martian foreshock. *Earth Planet. Phys.*, *9*(2), 357–365. http://doi.org/10.26464/epp2025027

**Abstract:** Ultra-low-frequency (ULF) waves are ubiquitous in terrestrial and planetary environments, playing a crucial role in energy transfer and dissipation through wave–particle interactions within space plasmas. By performing a detailed event study in terms of particle distribution maps and wave–particle variable correlation maps, we report that ULF waves observed by the Mars Atmosphere and Volatile EvolutioN (MAVEN) spacecraft in the Martian foreshock can effectively modulate the suprathermal electron fluxes by the magnetic field fluctuations. In particular, the variations in electron fluxes at energies of ~10–100 eV are significant in the perpendicular direction, showing good relationships with changes in the wave field strength characterized by a correlation coefficient ~0.8. These findings demonstrate the generality of interactions of ULF waves with electrons, even at these low energies, highlighting the importance of such processes throughout the heliosphere.

**Keywords:** Martian foreshock; ULF waves; electron modulation

## 1. Introduction

Ultra-low-frequency (ULF) waves, characterized by magnetic field fluctuations with frequencies below 1 Hz and sometimes extending down to millihertz (e.g., Zong QG et al., 2017), encompass various wave modes, including Alfvén waves, magnetosonic waves, mirror-mode waves, and occasionally whistler and ion cyclotron waves, depending on the plasma environment. These waves are commonly observed in the magnetospheres and magnetosheaths of Earth and other planets (e.g., Degeling et al., 2013; Dubinin and Fraenz, 2016; Shan LC et al., 2016; Harada et al., 2019; Jin TF et al., 2022), as well as in foreshock regions and the solar wind (Ala-Lahti et al., 2018; Salohub et al., 2022; Li JH et al., 2024). They are believed to play a crucial role in energy transfer and dissipation through wave–particle interactions with ions and electrons (Winningham et al., 2006; Zong QG et al., 2007; Rae et al., 2018; Zhao JT et al., 2022), leading to phenomena such as electron acceleration in radiation belts and ion scattering in the terrestrial magnetosphere (e.g., Su ZP et al., 2015; Ma X et al., 2020; Li XY et al., 2022; Shi XF et al., 2025).

Correspondence to: T. F. Jin, 00034286@whu.edu.cn
B. B. Ni, bbni@whu.edu.cn
Received 01 FEB 2025; Accepted 03 MAR 2025.
First Published online 05 MAR 2025.


A foreshock provides an ideal environment for ULF wave generation and growth. When the interplanetary magnetic field (IMF) connects to a bow shock, some solar wind particles are reflected at the shock surface and travel upstream along field lines (e.g., Eastwood et al., 2005). Such distributions of particle velocity are unstable and provide free energy for wave generation across a broad frequency range, including ULF waves (Mazelle et al., 2004; Wilson, 2016). Various kinds of ULF waves have been identified in foreshocks, often categorized by their period, such as "1-Hz" waves (Fairfield, 1969; Wong and Goldstein, 1988; Orlowski et al., 1995; Russell, 2007), "30-s" waves (Eastwood et al., 2004; Halekas et al., 2020), and "3-s" waves (Blanco-Cano, 2003; Wang S et al., 2021). These waves can further interact with local plasmas, accelerating or decelerating ions (Fu HS et al., 2009; He JS et al., 2019; Yao ST et al., 2021; Shi XF et al., 2025), or they can propagate downstream, modifying the plasma environment of the terrestrial magnetosphere (Kajdič et al., 2012; Takahashi et al., 2016; Turc et al., 2023), hence having great importance in understanding the phenomena in the foreshock region.

Despite the absence of a global dipole field, Mars possesses an induced magnetosphere formed by piled-up IMFs above the highly conductive Martian ionosphere (Nagy et al., 2004). A bow shock then forms close to the Martian surface, with an average subsolar altitude of ~0.58 $R_M$ ($R_M \approx 3389.5$ km is the radius of Mars; Vignes et al., 2000; Edberg et al., 2008). Similar to Earth's foreshock, the Martian foreshock is also abundant with wave activities covering a wide frequency range, including proton cyclotron waves (Wei HY and Russell, 2006; Romanelli et al., 2016), 1-Hz waves (Brain et al., 2002; Ruhunusiri et al., 2018; Jin TF et al., 2024), 3-s waves (Su ZP et al., 2023), and magnetosonic waves (Ruhunusiri et al., 2016; Shan LC et al., 2020; Pang SY et al., 2024). These waves can accelerate ions through wave–particle interactions, influencing ion escape from the Martian atmosphere (e.g., Dubinin et al., 2011; Lundin, 2011; Li SB et al., 2020).

Although being commonly observed, given their long period, ULF waves in the foreshock region are less known to have interactions with solar wind electrons because of the lower energy of the latter. Nevertheless, such interactions have been observed in the terrestrial foreshock (Chisham et al., 1996) and upstream of Halley's Comet (Larson et al., 1992), where electron fluxes appear to be modulated by the local magnetic field strength. A recent study describes an observation by the Magnetosphere Multi-Scale mission (Chen R et al., 2024), during which a series of large-amplitude ULF waves were detected, accompanied by variations in suprathermal electron (~10–100 eV) flux that correlated with the magnetic field. These suprathermal electrons, although a small population in the solar wind electrons, possess significantly higher kinetic energies than the core population (usually <10 eV). Dispersion analysis showed that the ULF wave-modified electron distributions could further generate simultaneously observed higher frequency waves. These observations suggest that ULF waves can interact with electrons, potentially regulating the foreshock plasma environment, offering an additional mechanism that might be responsible for solar wind energy dissipation in the foreshock region.

In this study, we report the observations of electron flux modulation by ULF waves in the Martian foreshock. The paper is organized as follows: In Section 2, we describe the datasets and the observed event. In Section 3, we analyze the suprathermal electron behavior and investigate its relationship with concurrent ULF wave activity. Section 4 summarizes the results with concluding remarks.

## 2. Event Observations

To investigate the relationship between low-frequency magnetic field fluctuations and solar wind electron variations, we utilize data from the Magnetometer (MAG; Connerney et al., 2015), Solar Wind Electron Analyzer (SWEA; Mitchell et al., 2016), and Solar Wind Ion Analyzer (SWIA; Halekas et al., 2013) instruments aboard the MAVEN spacecraft (Jakosky et al., 2015). The MAG provides magnetic field vector measurements, in both Mars Solar Orbital (MSO) and payload coordinate frames, at a sampling rate of up to 32 Hz. The SWEA provides three-dimensional (3D) differential flux measurements of electrons, with varying time resolutions depending on the data product. The SWIA "onboard moments" data are used to determine the solar wind velocity.

The case analyzed in this study was observed on August 14, 2015. The MAVEN spacecraft exited the Martian bow shock at approximately 22:09 universal time (UT), traveling from the northern hemisphere toward the equatorial plane along a trajectory near the subsolar meridian. At approximately 22:53 UT, MAVEN encountered a hot flow anomaly structure, after which wave activity at two distinct frequencies was observed simultaneously in the magnetic field data. These waves coincided with an enhancement of proton fluxes above 4 keV and variations in electron fluxes that were highly correlated with the ~0.04 Hz ULF waves. Figure 1 provides an overview of measurements, including magnetic field and electron data. During the plotted interval, the magnetic field exhibited persistent fluctuations primarily concentrated at ~0.4 Hz and ~0.04 Hz (Figure 1b), accompanied by periodic enhancements in suprathermal electron fluxes, identifiable by a gap near 10 eV in the electron energy spectrum (Figure 1c).

Unfortunately, the SWEA instrument did not return electron measurements at its highest time resolution on this day. As shown in Figures 1c and 1d, electron data on this day were unavailable until 23:03 UT, and the archived 3D data had a longer sampling period (8 s) than the survey pad data and spectrum data (both 4 s), which significantly limits our analysis. Figure 1e shows a magnified view of the electron energy spectrum during the time interval of ~23:07–23:12 UT, with the magnetic field strength overplotted. This interval was chosen for illustrative purposes. Clear correlations between differential flux and magnetic field strength are evident. Increases in $|\boldsymbol{B}|$ correspond to increases in electron fluxes above 10 eV, most notably between 20 and 50 eV, extending up to ~300 eV. Conversely, electron fluxes below 10 eV exhibit a more complex but anti-phased envelope curve. Electrons of ~710 eV increase in flux when $|\boldsymbol{B}|$ reaches its minimum, forming the upper edge of the anti-phased envelope. On the other hand, electrons of ~5–7 eV show flux enhancements correlated with $|\boldsymbol{B}|$, similar to the >10 eV electrons. It is noteworthy that the plotted energy spectrum may be affected by spacecraft potential, which can be corrected only during calculations over specific energy ranges. Figure 1f presents a more quantitative analysis, with the crimson and blue lines with circles representing partially integrated electron densities of <10 eV (crimson) and ~10–100 eV (blue). The two partial densities, particularly during periods of wave activity in the magnetic field, exhibit anti-correlated variation. Furthermore, each partial density is correlated with $|\boldsymbol{B}|$, implying modulation by the magnetic field.

Although high-resolution electron data are unavailable for much of this day, the 8-s sampling period of the archived 3D dataset nevertheless allowed us to analyze electron responses to magnetic field variations with a period of approximately 25 s. Figure 2 shows the pitch angle distribution of electrons in three different energy ranges during the interval of interest. We note that the energy shift attributable to spacecraft charging has been corrected in these plots. Electrons below 10 eV are concentrated in parallel directions, consistent with characteristics of the core population of solar wind electrons. Electrons of ~10–100 eV (as well as ~100–500 eV) begin to exhibit greater flux in anti-parallel directions, resembling features of the strahl component (e.g., Pierrard et al., 2001). Comparison of these distributions with the magnetic field strength shown in Figure 1e reveals that these periodic variations are correlated with $|\boldsymbol{B}|$. When the magnetic field is

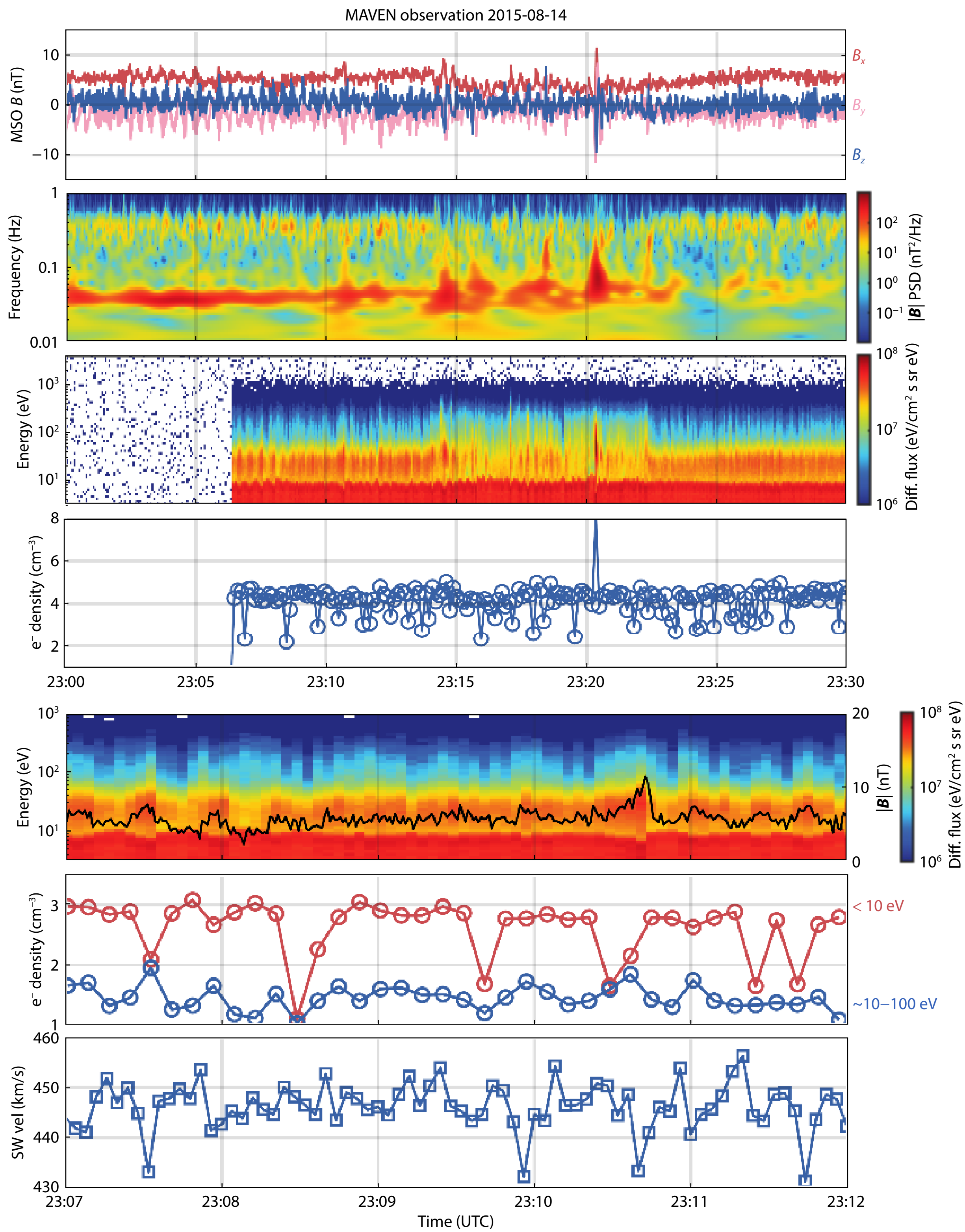


**Figure 1**. Overview of the event. (a–d): Measurements during the time interval of ~23:00–23:30. (a) Magnetic field measurement; (b) power density spectrum of |*B*|; (c) SWEA electron energy spectrum; (d) integrated electron density. (e–g): Time interval of ~23:07–23:12 magnified. (e) SWEA electron energy spectrum, with |*B*| overplotted (solid black line matching right ticks); (f) partially integrated electron density of <10 eV (crimson line with circles) and ~10–100 eV (blue line with circles); (g) solar wind velocity (SW vel) from the SWIA onboard moments data. PSD, phase space density.

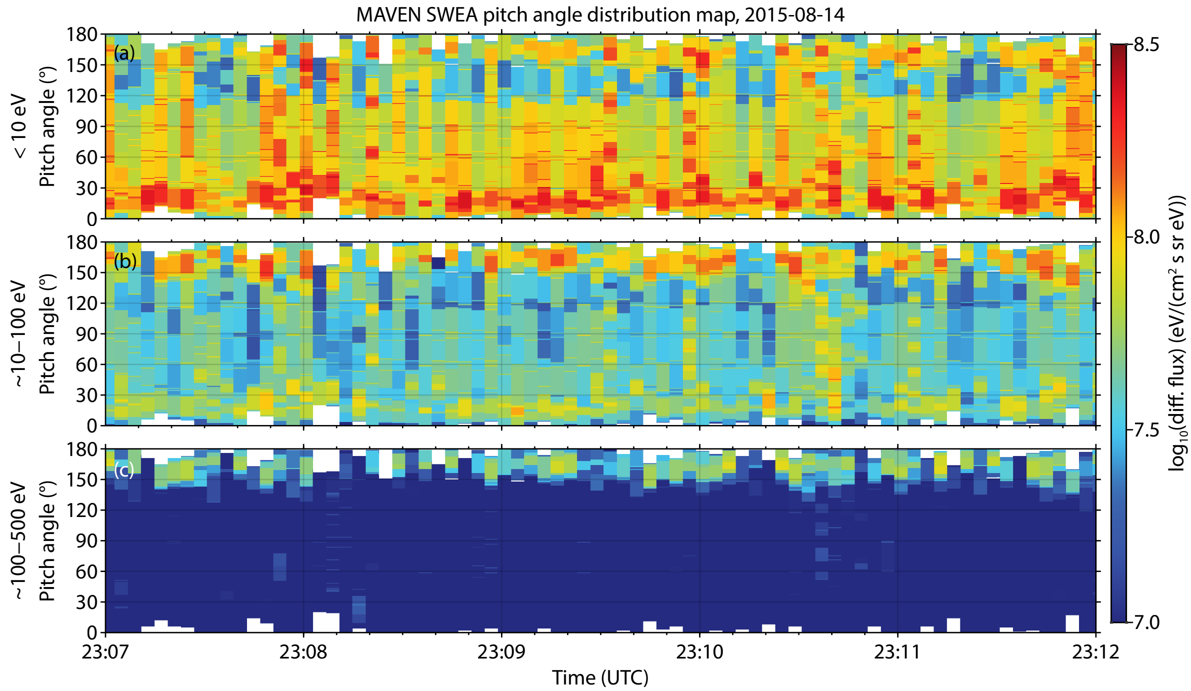


**Figure 2**. Pitch angle distributions of electron fluxes measured by the MAVEN SWEA during the time interval of ~23:07–23:12: (a) <10 eV; (b) ~10–100 eV; (c) ~100–500 eV.

enhanced, average fluxes in the perpendicular direction nearly double in magnitude. Although smaller than the field-aligned flux components, this periodic enhancement is still noticeable. More detailed analysis (examining each energy channel individually) reveals that the most significant contribution comes from electrons of ~30–55 eV. Meanwhile, the average fluxes of electrons below 10 eV, as well as the strahl electrons between 100 and 500 eV, exhibit periodicity, but with a weaker correlation to the magnetic field.

## 3. Analytic Results

To further analyze the relationships between electron behavior and magnetic field variations, we focus on a shorter interval, ~23:07–23:08 UT, during which the periodic variations in both magnetic field and electron data are most pronounced. Figures 3 and 4 present the SWEA instrument sky maps and electron velocity distributions in the mean-field and instrument frames, respectively.

Figure 3 displays the flux sky map of the SWEA instrument for electrons in different energy ranges during the interval of ~23:07–23:08 UT. The core population, concentrated in parallel directions (first column), and the strahl population, in anti-parallel directions (third column), are clearly visible. A noticeable enhancement in the second column, following the same pattern as the third column, indicates that the lower energy limit of the strahl electrons extends down to several tens of electron volts. The enhancement in perpendicular fluxes of ~10–100 eV electrons (second column) is evident at 23:07:00 UT (first row), 23:07:30 UT (fourth row), and 23:08:00 UT (last row). A comparison of the fourth row (23:07:30 UT) and the fifth row (23:07:40 UT) shows that this enhancement occurs uniformly across the plane perpendicular to the background magnetic field, rather than being concentrated in specific directions. This feature is even more pronounced for higher energy electrons (third column), whose fluxes are enhanced in nearly every sector compared with adjacent sampling periods.

We further calculate the PSD of ~10–100 eV electrons in the mean-field coordinate frame (Figure 4). Again, the enhancement of PSD in the perpendicular direction coincides with increases in $|\boldsymbol{B}|$, appearing as the darker crescents near $v_{B//}$ ~ 0 in Figures 4a, 4e, and 4h, as well as an overall increase in fluxes (compare Figures 4e and 4c to observe the shape enlargement). The PSD increase occurs across a broad range of parallel velocities. This PSD enhancement is consistent with the variations observed in the pitch angle distributions, suggesting that the electrons may be scattered into a wide range of pitch angles.

To quantify the relationships between the parameters of interest, we calculate the correlation coefficients for each pair of parameters. Because of the very different sampling rates of the dataset, all data are down-sampled to the time stamps of the electron density measurement by using spline interpolation. The calculated correlation coefficients are summarized in Figure 5. Several significant correlations are evident. The correlation between the total electron density and the density of electrons below 10 eV is clear, as these low-energy electrons comprise the core population of solar wind electrons. Similarly, the correlation between the density of ~10–100 eV electrons and the average flux of these electrons is also expected. It is notable that the magnetic field strength $|\boldsymbol{B}|$ correlates strongly with both the average fluxes and the density of ~10–100 eV electrons. The flux of these electrons in the perpendicular direction is particularly well correlated with $|\boldsymbol{B}|$. These results quantitatively confirm the modulation of $|\boldsymbol{B}|$ on the ~10–100 eV electron fluxes, primarily in the perpendicular direction. We also analyzed the band-passed $|\boldsymbol{B}|$, representing the ULF

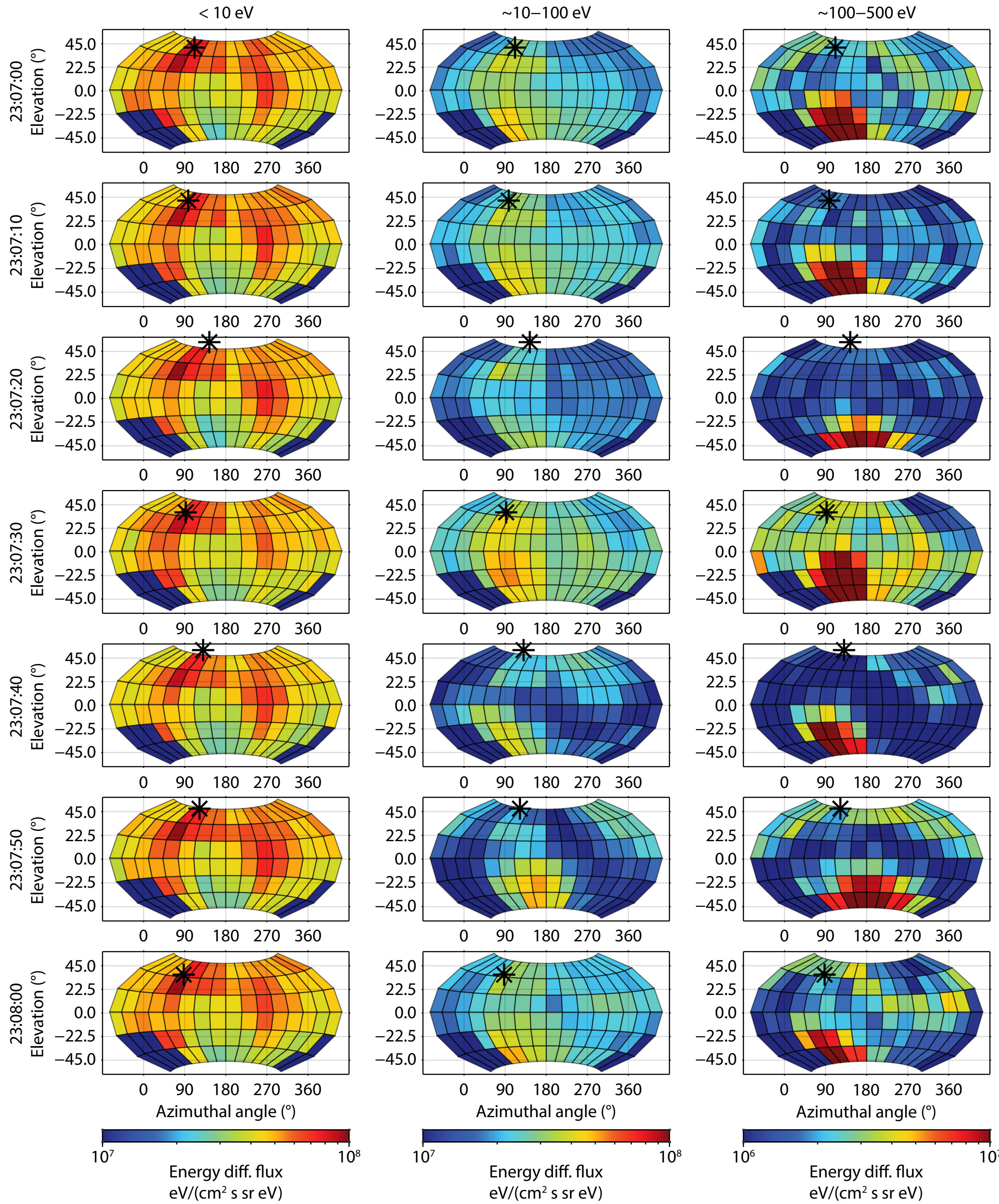


**Figure 3**. SWEA sky map of electron fluxes at energies of <10 eV (first column), ~10–100 eV (second column), and ~100–500 eV (third column) during the time interval of ~23:07–23:08.

fluctuations, and the angle between the IMF and the *x*-axis of the MSO coordinate frame, <***B***, *x*>. Interestingly, neither shows stronger correlations with other variables than |***B***| itself, although <***B***, *x*> is slightly better correlated with the solar wind and electron parameters than is the band-passed |***B***|.

## 4. Concluding Remarks

This study has examined the suprathermal electron behavior in the Martian foreshock observed by MAVEN on August 14, 2015. Through a comprehensive analysis of particle distribution and wave–particle variable correlation maps, we have shown that concurrent ULF waves effectively modulate suprathermal electron fluxes via magnetic field fluctuations. Specifically, the ~10–100 eV electron flux enhancements in the perpendicular direction (by a factor of ~2) are strongly related to changes in magnetic field strength (an increase of ~3 nT), with a correlation coefficient of ~0.8.

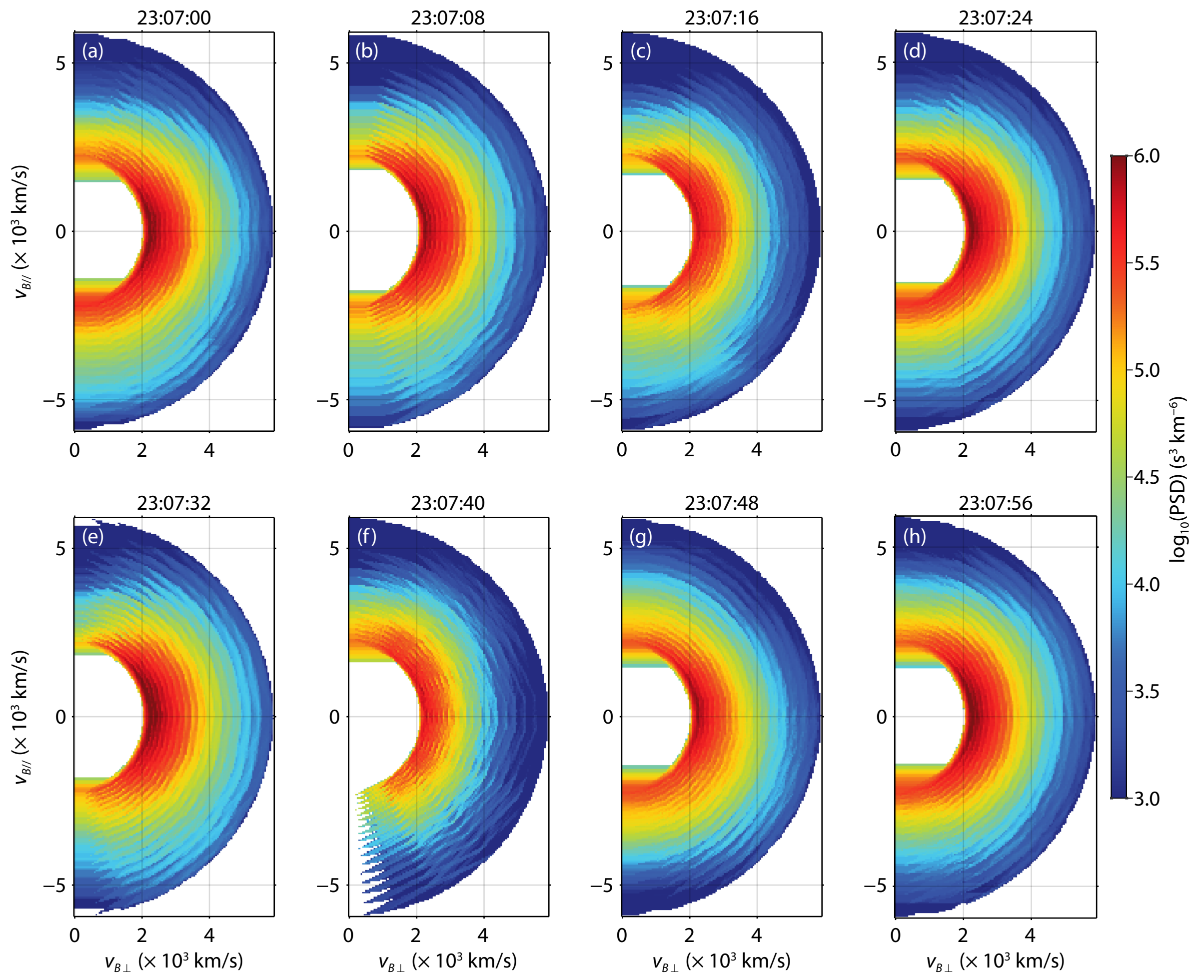


**Figure 4**. Velocity distribution maps of electron phase space density (PSD) for the energy range of ~10–100 eV during the time interval of ~23:07–23:08. Each subplot from (a) to (h) represents one sampling period, the calculated PSD projected in the mean-field coordinate frame (*x*-axis being the perpendicular velocity, and *y*-axis being the parallel velocity), with colors indicating the log values of PSD.

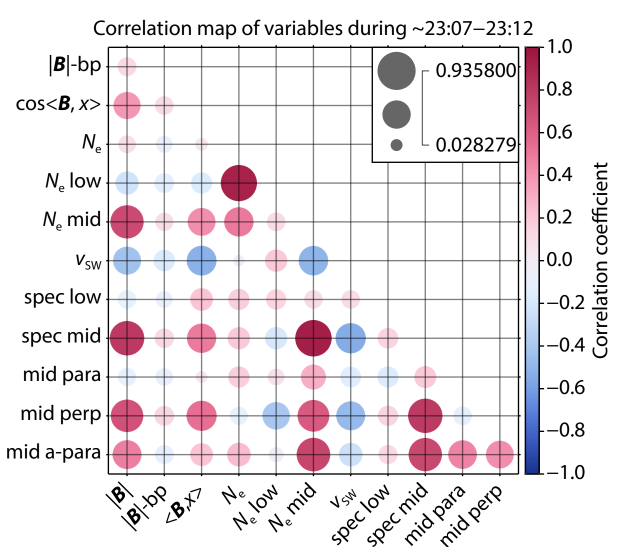


**Figure 5**. Correlation map of variables during the time interval of ~23:07–23:12. Each variable represents a physical parameter, as listed in Table 1. The color of each circle represents the value of the correlation coefficient, whereas the size of the circle represents the absolute value of the correlation coefficient.

**Table 1**. Names of variables and the physical parameters they represent, as plotted in Figure 5.

| Variable | Physical parameter |
|---|---|
| \|***B***\| | Magnetic field strength |
| \|***B***\|-bp | Band-passed \|***B***\| |
| <***B***, *x*> | Angle between ***B*** and the MSO *x*-axis |
| $N_e$ | Electron density |
| $N_e$ low | Partially integrated electron density of <10 eV |
| $n_e$ mid | Partially integrated electron density of ~10–100 eV |
| $v_{SW}$ | Solar wind velocity |
| spec low | Averaged differential flux of ~0–10 eV electrons |
| spec mid | Averaged differential flux of ~10–100 eV electrons |
| mid para | Averaged differential flux of ~10–100 eV electrons in the parallel direction (~0°–45°) |
| mid perp | Averaged differential flux of ~10–100 eV electrons in the perpendicular direction (~60°–120°) |
| mid a-para | Averaged differential flux of ~10–100 eV electrons in the anti-parallel direction (~135°–180°) |

One possible explanation for the observed modulation of ~10–100 eV electron fluxes can be associated with the conservation of the first adiabatic invariant. Given the definition of the magnetic moment, $\mu = E\sin^2\alpha/B$, where $E$ is the electron energy, $\alpha$ the electron pitch angle, and $B$ the ULF magnetic field strength, either $E$ or $\sin^2\alpha$ should vary in the same way if $\mu$ is conserved during variations in the wave magnetic field. In this event, the magnetic field strength increases by nearly 50% over one wave period (from ~5 to ~8 nT). If electron energy were conserved, pitch angle changes would be required to conserve $\mu$. That is, an electron with a pitch angle of ~90° at the $|\boldsymbol{B}|$ maximum should have a pitch angle of ~56° at the $|\boldsymbol{B}|$ minimum. However, no significant flux increase is observed around this pitch angle in any energy range during the wave period, suggesting that the changes in pitch angle alone are insufficient to maintain $\mu$ conservation. This result implies that electron heating (or energization) occurs during this modulation process.

The correlation between suprathermal electrons and the ULF wave magnetic field reported here is similar to that observed near the bow shock of Halley's Comet (Larson et al., 1992). A small parallel component of electron velocity can significantly contribute to increases in electron energy. A recent observation in the terrestrial foreshock (Chen R et al., 2024) also reported a similar event, where both low-frequency waves at ~0.2 Hz and higher frequency whistler mode waves (0.1–0.5 $f_{ce}$) occurred simultaneously to modulate ~10–100 eV electron fluxes. Chen R et al. (2024) attributed the modulation to adiabatic electron heating when the magnetic field is compressed by low-frequency waves with large amplitudes. In the study by Chen R et al. (2024), the electrons after the modulation are capable of exciting high-frequency whistler mode waves, whereas in our study, it is the ULF waves rather than 1-Hz waves that are generated locally. The similarity between these studies highlights the generality of these wave–particle interaction processes in the heliosphere, which surely requires intensive investigation in future studies.

## Acknowledgments

This research was supported by the National Natural Science Foundation of China (Grant Nos. 42188101, 42174188, 42474217, 42330207, 42374193, 42241143, and 42025404) and the National Key R&D Program of China (Grant Nos. 2022YFF0503700 and 2022YFF0503900). The data used in this study were provided by the MAVEN team (https://lasp.colorado.edu/maven/sdc/public/data/sci/) and the NASA Planetary Data System (PDS, https://pds-ppi.igpp.ucla.edu/). MAVEN MAG (Connerney, 2024), SWIA (Halekas, 2024), and SWEA (Mitchell, 2024) data were utilized in this study.

## References

Ala-Lahti, M. M., Kilpua, E. K. J., Dimmock, A. P., Osmane, A., Pulkkinen, T., and Souček, J. (2018). Statistical analysis of mirror mode waves in sheath regions driven by interplanetary coronal mass ejection. *Ann. Geophys.*, *36*(3), 793–808. https://doi.org/10.5194/angeo-36-793-2018

Blanco-Cano, X., Russell, C. T., Ramírez, J., and Le, G. (2003). Three second waves observed upstream of the Earth's bow shock. *AIP Conf. Proc.*, *679*(1), 501–504. https://doi.org/10.1063/1.1618644

Brain, D. A., Bagenal, F., Acuña, M. H., Connerney, J. E. P., Crider, D. H., Mazelle, C., Mitchell, D. L., and Ness, N. F. (2002). Observations of low-frequency electromagnetic plasma waves upstream from the Martian shock. *J. Geophys. Res.: Space Phys.*, *107*(A6), 1076. https://doi.org/10.1029/2000ja000416

Chen, R., Gao, X. L., Yang, Z. W., Lu, Q. M., Kong, Z. Y., Ma, J. Q., Ke, Y. G., and Wang, C. (2024). Cross-scale energy transfer from ion-scale to electron-scale waves in the Earth's foreshock region. *J. Geophys. Res.: Space Phys.*, *129*(7), e2024JA032567. https://doi.org/10.1029/2024JA032567

Chisham, G., Schwartz, S. J., and Burgess, D. (1996). The anisotropy variations of electron distributions in the terrestrial ion foreshock. *J. Geophys. Res.: Space Phys.*, *101*(A1), 445–455. https://doi.org/ https://doi.org/10.1029/95ja03128

Connerney, J. E. P., Espley, J., Lawton, P., Murphy, S., Odom, J., Oliversen, R., and Sheppard, D. (2015). The MAVEN magnetic field investigation. *Space Sci. Rev.*, *195*(1-4), 257–291. https://doi.org/10.1007/s11214-015-0169-4

Connerney, J. E. P. (2024). MAVEN Magnetometer (MAG) Calibrated Data Bundle. *NASA Planetary Data System*, https://doi.org/10.17189/1414178

Degeling, A. W., Rankin, R., Murphy, K., and Rae, I. J. (2013). Magnetospheric convection and magnetopause shadowing effects in ULF wave-driven energetic electron transport. *J. Geophys. Res.: Space Phys.*, *118*(6), 2919–2927. https://doi.org/10.1002/jgra.50219

Dubinin, E., Fraenz, M., Fedorov, A., Lundin, R., Edberg, N., Duru, F., and Vaisberg, O. (2011). Ion energization and escape on Mars and Venus. *Space Sci. Rev.*, *162*(1-4), 173–211. https://doi.org/10.1007/s11214-011-9831-7

Dubinin, E., and Fraenz, M. (2016). Ultra-low-frequency waves at Venus and Mars. In A. Keiling, et al. (Eds.), *Low-Frequency Waves in Space Plasmas* (pp. 343–364). Washington, DC: American Geophysical Union. https://doi.org/10.1002/9781119055006.ch20

Eastwood, J. P., Balogh, A., Mazelle, C., Dandouras, I., and Rème, H. (2004). Oblique propagation of 30 s period fast magnetosonic foreshock waves: A cluster case study. *Geophys. Res. Lett.*, *31*(4), L04804. https://doi.org/10.1029/2003gl018897

Eastwood, J. P., Lucek, E. A., Mazelle, C., Meziane, K., Narita, Y., Pickett, J., and Treumann, R. A. (2005). The foreshock. *Space Sci. Rev.*, *118*(1-4), 41–94. https://doi.org/10.1007/s11214-005-3824-3

Edberg, N. J. T., Lester, M., Cowley, S. W. H., and Eriksson, A. I. (2008). Statistical analysis of the location of the Martian magnetic pileup boundary and bow shock and the influence of crustal magnetic fields. *J. Geophys. Res.: Space Phys.*, *113*(A8), A08206. https://doi.org/10.1029/2008ja013096

Fairfield, D. H. (1969). Bow shock associated waves observed in the far upstream interplanetary medium. *J. Geophys. Res.*, *74*(14), 3541–3553. https://doi.org/10.1029/JA074i014p03541

Fu, H. S., Cao, J. B., Yang, B., Lucek, E., Rème, H., and Dandouras, I. (2009). ULF waves associated with solar wind deceleration in the Earth's foreshock. *Chin. Phys. Lett.*, *26*(11), 119402. https://doi.org/10.1088/0256-307X/26/11/119402

Halekas, J. S. (2024). MAVEN SWIA Calibrated Data Bundle. *NASA Planetary Data System*, https://doi.org/10.17189/1414182

Halekas, J. S., Taylor, E. R., Dalton, G., Johnson, G., Curtis, D. W., McFadden, J. P., Mitchell, D. L., Lin, R. P., and Jakosky, B. M. (2013). The solar wind ion analyzer for MAVEN. *Space Sci. Rev.*, *195*(1-4), 125–151. https://doi.org/10.1007/s11214-013-0029-z

Halekas, J. S., Ruhunusiri, S., Vaisberg, O. L., Harada, Y., Espley, J. R., Mitchell, D. L., Mazelle, C., Romanelli, N., DiBraccio, G. A., and Brain, D. A. (2020). Properties of plasma waves observed upstream from Mars. *J. Geophys. Res.: Space Phys.*, *125*(9), e2020JA028221. https://doi.org/10.1029/2020ja028221

Harada, Y., Ruhunusiri, S., Halekas, J. S., Espley, J., DiBraccio, G. A., Mcfadden, J. P., Mitchell, D. L., Mazelle, C., Collinson, G., … Jakosky, B. M. (2019). Locally generated ULF waves in the Martian magnetosphere: MAVEN observations. *J. Geophys. Res.: Space Phys.*, *124*(11), 8707–8726. https://doi.org/10.1029/2019ja027312

He, J. S., Duan, D., Zhu, X. Y., Yan, L. M., and Wang, L. H. (2019). Observational evidences of wave excitation and inverse cascade in a distant Earth foreshock region. *Sci. China Earth Sci.*, *62*(4), 619–630. https://doi.org/10.1007/s11430-019-9330-3

Jakosky, B. M., Lin, R. P., Grebowsky, J. M., Luhmann, J. G., Mitchell, D. F., Beutelschies, G., Priser, T., Acuna, M., Andersson, L., … Zurek, R. (2015). The *Mars atmosphere and volatile evolution* (*MAVEN*) mission. *Space Sci. Rev.*, *195*(1-4), 3–48. https://doi.org/10.1007/s11214-015-0139-x

Jin, T. F., Lei, L., Yiteng, Z., Lianghai, X., and Fuhao, Q. (2022). Statistical analysis of the distribution and evolution of mirror structures in the Martian magnetosheath. *Astrophys. J.*, *929*(2), 165. https://doi.org/10.3847/1538-4357/ac5f00

Jin, T. F., Ni, B. B., Fu, S., Li, L., Cao, X., Pang, S. Y., Yun, X. T., Long, M. Y., and Du, H. L. (2024). Unusually low-frequency whistler-mode waves and their association with high-energy protons observed upstream of Martian bow shock. *Astrophys. J.*, *966*(1), 64. https://doi.org/10.3847/1538-4357/ad333d

Kajdič, P., Blanco-Cano, X., Aguilar-Rodriguez, E., Russell, C. T., Jian, L. K., and Luhmann, J. G. (2012). Waves upstream and downstream of interplanetary shocks driven by coronal mass ejections. *J. Geophys. Res.: Space Phys.*, *117*(A6), A06103. https://doi.org/10.1029/2011ja017381

Larson, D. E., Anderson, K. A., Lin, R. P., Carlson, C. W., Réme, H., Glassmeier, K. H., and Neubauer, F. M. (1992). Electron distributions upstream of the comet Halley bow shock: Evidence for adiabatic heating. *J. Geophys. Res.: Space Phys.*, *97*(A3), 2907–2916. https://doi.org/10.1029/91ja02698

Li, J. H., Zhou, X. Z., Liu, Z. Y., Wang, S., Artemyev, A. V., Omura, Y., Zhang, X. J., Li, L., Yue, C., … Burch, J. L. (2024). Identification of coupled Landau and anomalous resonances in space plasmas. *Phys. Rev. Lett.*, *133*(3), 035201. https://doi.org/10.1103/PhysRevLett.133.035201

Li, S. B., Lu, H. Y., Cui, J., Yu, Y. Q., Mazelle, C., Li, Y., and Cao, J. B. (2020). Effects of a dipole-like crustal field on solar wind interaction with Mars. *Earth Planet. Phys.*, *4*(1), 23–31. https://doi.org/10.26464/epp2020005

Li, X. Y., Liu, Z. Y., Zong, Q. G., Liu, J. J., Fu, S. Y., Zhou, X. Z., Hao, Y. X., Pollock, C. J., Russell, C. T., … Lindqvist, P. A. (2022). ULF wave-induced ion pitch angle evolution in the dayside outer magnetosphere. *Geophys. Res. Lett.*, *49*(8), e2022GL098108. https://doi.org/10.1029/2022gl098108

Lundin, R. (2011). Ion acceleration and outflow from Mars and Venus: An overview. *Space Sci. Rev.*, *162*(1-4), 309–334. https://doi.org/10.1007/s11214-011-9811-y

Ma, X., Xiang, Z., Ni, B. B., Fu, S., Cao, X., Hua, M., Guo, D. Y., Guo, Y. J., Gu, X. D., … Zhu, Q. (2020). On the loss mechanisms of radiation belt electron dropouts during the 12 September 2014 geomagnetic storm. *Earth Planet. Phys.*, *4*(6), 598–610. https://doi.org/10.26464/epp2020060

Mazelle, C., Winterhalter, D., Sauer, K., Trotignon, J. G., Acuña, M. H., Baumgärtel, K., Bertucci, C., Brain, D. A., Brecht, S. H., … Slavin, J. (2004). Bow shock and upstream phenomena at Mars. *Space Sci. Rev.*, *111*(1-2), 115–181. https://doi.org/10.1023/B:SPAC.0000032717.98679.d0

Mitchell, D. L. (2024), MAVEN SWEA calibrated data bundle. *NASA Planetary Data System*, https://doi.org/10.17189/7cx9-xy68

Mitchell, D. L., Mazelle, C., Sauvaud, J. A., Thocaven, J. J., Rouzaud, J., Fedorov, A., Rouger, P., Toublanc, D., Taylor, E., … Jakosky, B. M. (2016). The MAVEN solar wind electron analyzer. *Space Sci. Rev.*, *200*(1-4), 495–528. https://doi.org/10.1007/s11214-015-0232-1

Nagy, A. F., Winterhalter, D., Sauer, K., Cravens, T. E., Brecht, S., Mazelle, C., Crider, D., Kallio, E., Zakharov, A., … Trotignon, J. G. (2004). The plasma environment of Mars. *Space Sci. Rev.*, *111*(1-2), 33–114. https://doi.org/10.1023/b:Spac.0000032718.47512.92

Orlowski, D. S., Russell, C. T., Krauss-Varban, D., Omidi, N., and Thomsen, M. F. (1995). Damping and spectral formation of upstream whistlers. *J. Geophys. Res.: Space Phys.*, *100*(A9), 17117–17128. https://doi.org/10.1029/95ja00062

Pang, S. Y., Fu, S., Yun, X. T., Jin, T. F., Cao, X., Du, H. L., and Ma, X. (2024). Global distribution of Martian upstream magnetosonic waves observed by MAVEN. *J. Geophys. Res.: Planets*, *129*(12), e2024JE008410. https://doi.org/10.1029/2024je008410

Pierrard, V., Maksimovic, M., and Lemaire, J. (2001). Core, halo and strahl electrons in the solar wind. *Astrophys. Space Sci.*, *277*(1-2), 195–200. https://doi.org/10.1023/A:1012218600882

Rae, I. J., Murphy, K. R., Watt, C. E. J., Halford, A. J., Mann, I. R., Ozeke, L. G., Sibeck, D. G., Clilverd, M. A., Rodger, C. J., … Singer, H. J. (2018). The role of localized compressional ultra-low frequency waves in energetic electron precipitation. *J. Geophys. Res.: Space Phys.*, *123*(3), 1900–1914. https://doi.org/10.1002/2017ja024674

Romanelli, N., Mazelle, C., Chaufray, J. Y., Meziane, K., Shan, L., Ruhunusiri, S., Connerney, J. E. P., Espley, J. R., Eparvier, F., … Jakosky, B. M. (2016). Proton cyclotron waves occurrence rate upstream from Mars observed by MAVEN: Associated variability of the Martian upper atmosphere. *J. Geophys. Res.: Space Phys.*, *121*(11), 11113–11128. https://doi.org/10.1002/2016ja023270

Ruhunusiri, S., Halekas, J. S., Connerney, J. E. P., Espley, J. R., McFadden, J. P., Mazelle, C., Brain, D., Collinson, G., Harada, Y., … and Jakosky, B. M. (2016). MAVEN observation of an obliquely propagating low-frequency wave upstream of Mars. *J. Geophys. Res.: Space Phys.*, *121*(3), 2374–2389. https://doi.org/10.1002/2015ja022306

Ruhunusiri, S., Halekas, J. S., Espley, J. R., Eparvier, F., Brain, D., Mazelle, C., Harada, Y., DiBraccio, G. A., Thiemann, E. M. B., … Sulaiman, A. H. (2018). One-hertz waves at Mars: MAVEN observations. *J. Geophys. Res.: Space Phys.*, *123*(5), 3460–3476. https://doi.org/10.1029/2017ja024618

Russell, C. T. (2007). Upstream whistler-mode waves at planetary bow shocks: A brief review. *J. Atmos. Sol.: Terr. Phys.*, *69*(14), 1739–1746. https://doi.org/10.1016/j.jastp.2006.11.004

Salohub, A., Šafránková, J., Němeček, Z., Němec, F., and Pi, G. (2022). ULF waves/fluctuations in the distant foreshock: Statistical approach. *J. Geophys. Res.: Space Phys.*, *127*(12), e2022JA030802. https://doi.org/10.1029/2022JA030802

Shan, L. C., Mazelle, C., Meziane, K., Delva, M., Lu, Q. M., Ge, Y. S., Du, A. M., and Zhang, T. L. (2016). Characteristics of quasi-monochromatic ULF waves in the Venusian foreshock. *J. Geophys. Res.: Space Phys.*, *121*(8), 7385–7397. https://doi.org/10.1002/2016ja022876

Shan, L. C., Ge, Y. S., and Du, A. M. (2020). A case study of large-amplitude ULF waves in the Martian foreshock. *Earth Planet. Phys.*, *4*(1), 45–50. https://doi.org/10.26464/epp2020004

Shi, X. F., Artemyev, A., Angelopoulos, V., Liu, T., and Wilson Iii, L. B. (2025). Compound electron acceleration at planetary foreshocks. *Nat. Commun.*, *16*(1), 77. https://doi.org/10.1038/s41467-024-55464-8

Su, Z. P., Zhu, H., Xiao, F. L., Zong, Q. G., Zhou, X. Z., Zheng, H. N., Wang, Y. M., Wang, S., Hao, Y. X., … Wygant, J. R. (2015). Ultra-low-frequency wave-driven diffusion of radiation belt relativistic electrons. *Nat. Commun.*, *6*(1), 10096. https://doi.org/10.1038/ncomms10096

Su, Z. P., Wang, Y. M., Zhang, T. L., Wu, Z. Y., Cheng, L., Zou, Z. X., Shen, C. L., Guo, J. N., Xiao, S. D., … and Xu, M. J. (2023). Unusual Martian foreshock waves triggered by a solar wind stream interaction region. *Astrophys. J. Lett.*, *947*(2). https://doi.org/10.3847/2041-8213/accb9f

Takahashi, K., Hartinger, M. D., Malaspina, D. M., Smith, C. W., Koga, K., Singer, H. J., Frühauff, D., Baishev, D. G., Moiseev, A. V., and Yoshikawa, A. (2016). Propagation of ULF waves from the upstream region to the midnight sector of the inner magnetosphere. *J. Geophys. Res.: Space Phys.*, *121*(9), 8428–8447. https://doi.org/10.1002/2016ja022958

Turc, L., Roberts, O. W., Verscharen, D., Dimmock, A. P., Kajdič, P., Palmroth, M., Pfau-Kempf, Y., Johlander, A., Dubart, M., … and Ganse, U. (2023). Transmission of foreshock waves through Earth's bow shock. *Nat. Phys.*, *19*(1), 78–86. https://doi.org/10.1038/s41567-022-01837-z

Vignes, D., Mazelle, C., Rme, H., Acuña, M. H., Connerney, J. E. P., Lin, R. P., Mitchell, D. L., Cloutier, P., Crider, D. H., and Ness, N. F. (2000). The solar wind interaction with Mars: Locations and shapes of the bow shock and the magnetic pile-up boundary from the observations of the MAG/ER Experiment onboard Mars Global Surveyor. *Geophys. Res. Lett.*, *27*(1), 49–52. https://doi.org/10.1029/1999gl010703

Wang, S., Chen, L. J., Ng, J., Bessho, N., Le, G., Fung, S. F., Gershman, D. J., and Giles, B. L. (2021). A statistical study of three-second foreshock ULF waves observed by the Magnetospheric Multiscale mission. *Phys. Plasmas*, *28*(8), 082901. https://doi.org/10.1063/5.0055972

Wei, H. Y., and Russell, C. T. (2006). Proton cyclotron waves at Mars: Exosphere structure and evidence for a fast neutral disk. *Geophys. Res. Lett.*, *33*(23). https://doi.org/10.1029/2006gl026244

Wilson, L. B., III. (2016). Low frequency waves at and upstream of collisionless shocks. In A. Keiling, et al. (Eds.), *Low-Frequency Waves in Space Plasmas* (pp. 269–291). American Geophysical Union, John Wiley & Sons, Inc. https://doi.org/10.1002/9781119055006.ch16

Winningham, J. D., Frahm, R. A., Sharber, J. R., Coates, A. J., Linder, D. R., Soobiah, Y., Kallio, E., Espley, J. R., Lundin, R., … Dierker, C. (2006). Electron oscillations in the induced Martian magnetosphere. *Icarus*, *182*(2), 360–370. https://doi.org/10.1016/j.icarus.2005.10.033

Wong, H. K., and Goldstein, M. L. (1988). Proton beam generation of oblique whistler waves. *J. Geophys. Res.: Space Phys.*, *93*(A5), 4110–4114. https://doi.org/10.1029/JA093iA05p04110

Yao, S. T., Shi, Q. Q., Zong, Q. G., Degeling, A. W., Guo, R. L., Li, L., Li, J. X., Tian, A. M., Zhang, H., … Pollock, C. J. (2021). Low-frequency whistler waves modulate electrons and generate higher-frequency whistler waves in the solar wind. *Astrophys. J.*, *923*(2), 216. https://doi.org/10.3847/1538-4357/ac2e97

Zhao, J. T., Zong, Q. G., Yue, C., Zhou, X. Z., Liu, Z. Y., Sun, W. J., Slavin, J. A., Raines, J. M., and Zhu, X. Y. (2022). ULF modulations on plasma environment and coherent waves of Mercury's magnetosphere: MESSENGER's observation. *J. Geophys. Res.: Space Phys.*, *127*(9), e2021JA030253. https://doi.org/10.1029/2021ja030253

Zong, Q. G., Zhou, X. Z., Li, X., Song, P., Fu, S. Y., Baker, D. N., Pu, Z. Y., Fritz, T. A., Daly, P., … Réme, H. (2007). Ultralow frequency modulation of energetic particles in the dayside magnetosphere. *Geophys. Res. Lett.*, *34*(12), L12105. https://doi.org/10.1029/2007gl209915

Zong, Q. G., Rankin, R., and Zhou, X. Z. (2017). The interaction of ultra-low-frequency pc3–5 waves with charged particles in Earth's magnetosphere. *Rev. Mod. Plasma Phys.*, *1*(1), 10. https://doi.org/10.1007/s41614-017-0011-4